Mechanism and Machine Theory 200 (2024) 105704

Contents lists available at ScienceDirect

Mechanism and Machine Theory

journal homepage: www.elsevier.com/locate/mechmt

Research paper

Softening nonlinear-stiffness elastic mechanism with continuous adjustability for human–robot interaction force control

Zhixin Tu [a], Haifeng Liu [a], Yihao Jiang [a], Tao Ye [a], Yuepeng Qian [a], Yuquan Leng [a], Jian S. Dai [a,b], Chenglong Fu [a,*]

[a] Shenzhen Key Laboratory of Biomimetic Robotics and Intelligent Systems and Guangdong Provincial Key Laboratory of Human-Augmentation and Rehabilitation Robotics in Universities, Southern University of Science and Technology, Shenzhen, 518055, Guangdong, China
[b] Centre for Robotics Research, King's College London, London WC2R 2LS, United Kingdom

ARTICLE INFO

Keywords:
Elastic mechanism
Nonlinear stiffness
Softening stiffness behavior
Adjustable stiffness profile
Human–robot interaction force control

ABSTRACT

Human–robot interaction of human augmentation robots presents a considerable challenge in achieving accurate and robust interaction force control. This paper proposes a novel softening nonlinear elastic mechanism with continuous adjustability (SNEMA) to address this challenge. The SNEMA achieves softening stiffness behavior through a nonlinear mapping relationship between the lengths of the diamond diagonals. This unique stiffness profile, featuring high stiffness for low output and low stiffness for high output, strikes a balance between the output force range and force resolution. Moreover, the continuous and convenient adjustment of the stiffness profile is realized by utilizing two antagonistic linear springs, enabling optimal stiffness matching for different output force ranges. Bench tests were conducted to validate the stiffness modeling and evaluate the force tracking and interaction performance of the developed SNEMA. Experimental results demonstrate the capability of the SNEMA to achieve precise force control and good collision safety in human–robot interaction. The proposed SNEMA is finally deployed on the Centaur robot to demonstrate its advantages in practical application.

1. Introduction

Recent advancements in human augmentation robots [1–10] have led to the development of systems designed to assist or enhance human capabilities. These robots effectively reduce the energy consumption of individuals in daily activities by providing additional aiding torque or force. One prominent example is the human locomotion process, where some joint exoskeletons [1–7] assist human walking by providing joint torque assistance. Joint exoskeletons mimic the distribution of biological torque to reduce the natural force of the human. However, studies have shown that joint-level assistance is not the optimal choice to reduce metabolic rate. The forward aiding force applied at the center of mass (COM) can reduce walking metabolism by up to 48% [11,12]. A novel form of human augmentation robot, supernumerary robotic limbs (SRLs) [8–10], has introduced a new way to assist the human. They are developed to collaborate with the human as an independent agent, not being attached to the human torso or joints. In our previous work [13,14], a wearable lower-limb SRLs, Centaur robot, was proposed to assist human walking with load-carriage, as shown in Fig. 1(a). The decoupled robotic legs of the Centaur robot can share the load weight while simultaneously propelling the robot's torso, providing assistance force between the human and the robot. However, for these collaborative human augmentation robots [8,10,13,14], the presence of a rigid connection structure engenders a considerable mechanical impedance between the human and the robotic systems. In addition, the complexity of modeling and predicting human stiffness and motion, coupled with

* Corresponding author.
E-mail addresses: 12131094@mail.sustech.edu.cn (Z. Tu), fucl@sustech.edu.cn (C. Fu).

https://doi.org/10.1016/j.mechmachtheory.2024.105704
Received 2 May 2024; Received in revised form 1 June 2024; Accepted 1 June 2024
Available online 8 June 2024

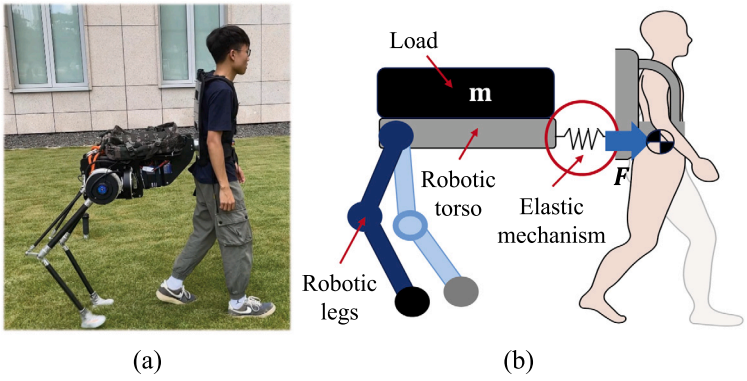

Fig. 1. Centaur robot prototype and schematic illustration of introducing the elastic mechanism between the human and the Centaur robot. (a) The prototype of the Centaur robot to help people walk with load-carriage [14]. (b) Schematic of human-Centaur system with an elastic mechanism. The incorporation of elastic mechanisms enables compliant human–robot interaction and transforms the interaction force control into the relative motion control between the human and the robot.

the difficulty of compensating for large mechanical impedance through algorithms, poses challenges in accurately controlling the interaction force between the human and the robot.

In the existing literature [15–18], compliance between humans and robots is essential for the performance of the human–robot interaction. Elastic mechanisms are regarded as the representatives of compliant mechanisms, which decouple robots from the human or the environment by introducing elastic components in order to achieve compliance interaction. The stable mechanical properties of elastic components also help to achieve precise control of human–robot interaction force. Series elastic actuator (SEA) [19–21] is the most typical compliant elastic mechanism, widely used in assistive robots for its excellent force and torque control ability. However, the constant stiffness is the main drawback of the SEA, as it cannot balance the different characteristics of low and high stiffness. Specifically, the usage of stiff springs in constant stiffness elastic mechanisms will increase the output force range and bandwidth but simultaneously decrease the accuracy of force control. On the contrary, using soft springs can improve the force resolution but reduces the response speed and requires larger space occupation for the same output force range. In addition, elastic components with fixed stiffness also perform poorly in energy efficiency [16,22], which further restricts their broader application in the aforementioned domain.

The elastic mechanism with nonlinear stiffness is a feasible solution to the above limitations, considering that the nonlinear stiffness can display different characteristics in different regions of the stiffness profile [2,3,23–33]. Aguirre-Ollinger et al. [23] designed an exoskeleton SEA, which connects the soft and stiff springs in series to demonstrate high stiffness characteristics after the soft spring is fully compressed. In [2,24,25], nonlinear elastic mechanisms were proposed to achieve the predefined stiffness profile by designing the contour of the cam profile. However, the stiffness profiles of these mechanisms are fixed and cannot be adjusted to accommodate varying requirements, rendering them unsuitable for different assistance levels or task scenarios. The adjustable elastic mechanisms are able to change the stiffness profile to improve flexibility and adaptability. Typically, the variable stiffness is achieved through the integration of an additional regulation motor and employing stiffness adjustment principles [26], such as adjusting the spring preload force [3,27,28] and the lever arm length [29–31]. These designs collectively allow for the real-time stiffness modulation. Nevertheless, the inclusion of an additional control unit in the variable stiffness mechanism introduces expensive energy consumption and bulky structure, thereby increasing the overall complexity of the control system. This is not ideal for compact human augmentation robots that prioritize simplicity and efficiency [16].

As an alternative, passive nonlinear elastic mechanisms with reconfigurability are introduced (e.g. RRSEAns [32] and JVSR [33]). RRSEAns [32] achieves adjustable nonlinear stiffness by using tension springs coupled to two coaxial rotating plates. The nonlinearity of the stiffness profile is adjusted by altering the offset angle or the pre-tension length between the spring pairs. JVSR [33] manually adjusts the spring preload and the number of cable windings on the pulley block to change the stiffness modes of the mechanism. These reconfigurable elastic mechanisms offer a simpler structure, lighter weight, and greater suitability for integration into human augmentation robots. However, their reconfigurability depends on specific spring arrangements and cable winding methods [34]. Achieving an adjustable stiffness profile requires disassembling the mechanism to alter the distribution and assembly of internal components. This design does not facilitate stiffness adjustments during operation, thereby limiting the mechanism's feasibility in practical application. Therefore, it is necessary to develop a simple, compact, and easily adjustable nonlinear elastic mechanism to overcome the limitations of existing adjustable elastic mechanisms.

Existing nonlinear elastic mechanisms predominantly adopt a hardening stiffness pattern [2,24,25,32], characterized by increasing stiffness with output force. The hardening stiffness is widely used in various joint-level assistive robots [2,4,23]. The low stiffness at low output meets the requirements for joint assistance transparency, while the high precision position control capability of motors [35] compensates for the loss of force resolution at high outputs. However, as a legged powered robot, the Centaur robot faces challenges in accurately controlling its torso due to the high dynamic walking impact and underactuated control characteristics [36].

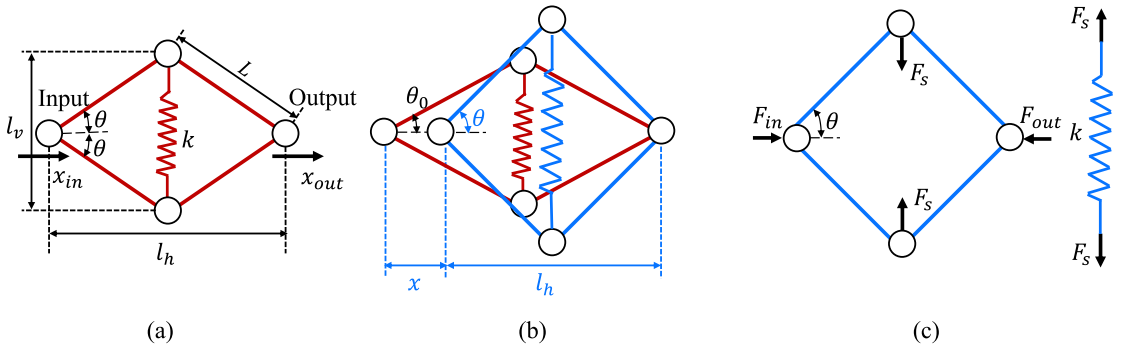

Fig. 2. (a) Conceptual schematic of the diamond-shaped SNEMA. (b) Kinematic diagram of the SNEMA. (c) Static force diagram of the SNEMA. (For interpretation of the references to color in this figure legend, the reader is referred to the web version of this article.)

This necessitates a higher force resolution within the target output range to achieve precise force control. Therefore, the softening stiffness profile is more suitable for the human-Centaur system. Softening stiffness achieves low stiffness within the high output range to ensure precise force control and collision safety [37], while achieving high stiffness in the low output to enhance responsiveness, minimize the mechanism stroke, and maintain a compact structure. However, current research and development of adjustable softening stiffness elastic mechanisms are relatively sparse. The JVSR [33] can demonstrate softening torque stiffness behavior when the spring preload force exceeds a certain threshold. But the adjustability range of the softening stiffness profile in JVSR is limited, and the specific characteristics of softening stiffness for interaction force control are not reported.

To address the limitations in the adjustability and stiffness behavior of existing elastic mechanisms, a novel softening nonlinear-stiffness elastic mechanism with continuous adjustability (SNEMA) is proposed in this paper for human–robot interaction force control. The SNEMA featured a diamond-shaped framework to generate a nonlinear force–displacement mapping relationship, resulting in a softening force stiffness profile that effectively balances the output force range and the force control precision while ensuring collision safety for human–robot interaction. Continuous and convenient adjustment of the stiffness profile is achieved by rotating the bolt of the antagonistic-spring regulation mechanism, enhancing flexibility and adaptability across various application scenarios. Moreover, the stiffness characteristics of the SNEMA are comprehensively modeled and analyzed, investigating the influence of various mechanical parameters on the stiffness characteristics. The analysis helps to provide guidance for the design of the stiffness profile and the selection of mechanical parameters. The bench tests and preliminary application experiment are conducted to validate the stiffness model, force tracking, and interaction characteristics of the proposed SNEMA, demonstrating the advantages of the softening stiffness in human–robot interaction force control.

The rest of the paper is organized as follows: Section 2 elucidates the conceptual design and stiffness modeling of the SNEMA. Section 3 introduces the adjustable stiffness profile and the parameter selection principle of the SNEMA. The physical implementation and mechanical design are presented in Section 4. Section 5 introduces the force control strategy and demonstrates the force tracking and interaction performance in varied stiffness. The preliminary application experiment of the SNEMA in the Centaur robot is introduced in Section 6. Finally, the discussion and conclusion are presented in Section 7, respectively.

2. Conceptualization and stiffness modeling of the SNEMA

2.1. Basic concept of the SNEMA

The proposed SNEMA, as depicted in Fig. 2(a), is conceptually designed as a diamond-shaped elastic mechanism. It comprises four links of equal length, four rotary joints, and a linear spring. The linear spring is attached to one of the diagonals of the diamond, referred to as the horizontal diagonal (HD), while the input and output ends of the mechanism are situated at the vertexes of the other diagonal, defined as vertical diagonal (VD). L indicates the length of the link, and the stiffness of the linear spring is indicated by k. The angle between the link and the HD of the mechanism is indicated by θ, and it is referred to as the mechanism angle in this work. l_h and l_v represent the length of the HD and VD, respectively. The displacements of the input and output ends along the HD, indicating translation movements, are marked as x_{in} and x_{out}, respectively, with the positive direction of displacement shown by black solid arrows. When the relative displacement occurs between the input end and the output end in the HD direction, the spring fixed on the VD undergoes deformation, generating force and establishing a nonlinear mapping relationship of the force between the diagonals of the diamond-shaped SNEMA. This results in the softening nonlinear-stiffness behavior of the SNEMA.

2.2. Kinematic principle and stiffness modeling

Fig. 2(b) shows the kinematic schematic of the proposed diamond-shaped SNEMA. The initial state of the SNEMA is defined as the condition where the entire mechanism is in a state of balance without external force, as shown by the red schematic in Fig. 2(b).

In the initial state, the length of the spring is at the original length, and the linear spring does not exert force on the mechanism. The lengths of both the diagonals can be calculated by

$$\begin{cases} l_{h0} = 2L\cos\theta_0 \\ l_{v0} = 2L\sin\theta_0 \end{cases}, \quad \theta_0 \in \left(0, \frac{\pi}{2}\right). \tag{1}$$

where l_{h0} and l_{v0} are the lengths of the HD and VD in the initial state, respectively; θ_0 is the mechanism angle in the initial state, ranging from 0 rad to $\frac{\pi}{2}$ rad.

To identify the motion state of the SNEMA, the variable x is defined as the difference between the initial length of HD and the current length of HD after the translation of the input and output ends. The calculation equation and range of x can be expressed as

$$x = l_{h0} - l_h, \quad x \in (2L\cos\theta_0 - 2L, 2L\cos\theta_0). \tag{2}$$

When x equals zero, the mechanism is in its initial state. A positive x value signifies that the mechanism is in a compressed state, whereas a negative x value indicates that the mechanism is in an extended state. The blue schematic diagram of Fig. 2(b) shows the kinematic state of the SNEMA when it is relatively compressed by x. The lengths of HD and VD can be determined by the following equations:

$$\begin{cases} l_h = 2L\cos\theta_0 - x \\ l_v = \sqrt{4L^2 - (2L\cos\theta_0 - x)^2} \end{cases}. \tag{3}$$

In this state, the static forces acting upon the SNEMA are depicted in Fig. 2(c). F_s represents the tension generated by the spring, while F_{in} and F_{out} correspond to the external equilibrium forces applied to the input and output ends. F_s can be expressed according to Hooke's law as

$$F_s = k \cdot (l_v - l_{v0}) = k \cdot \sqrt{4L^2 - (2L\cos\theta_0 - x)^2} - k \cdot 2L\sin\theta_0. \tag{4}$$

Based on the geometric properties and the parallelogram law of force, it can be deduced that the ratio of F_s to F_{out} is equal to the ratio of the corresponding diagonal lengths. This relationship can be expressed as follows:

$$\frac{F_s}{F_{out}} = \frac{l_v}{l_h}. \tag{5}$$

Substituting Eqs. (3) and (4) into Eq. (5) and rearranging it, the output force F_{out} can be calculated by

$$F_{out} = k \cdot (2L\cos\theta_0 - x) - \frac{2kL\sin\theta_0(2L\cos\theta_0 - x)}{\sqrt{4L^2 - (2L\cos\theta_0 - x)^2}}, \tag{6}$$

where we can observe that the output force F_{out} of the SNEMA is dependent on the initial state parameters θ_0, L, and k. All these three parameters are the mechanical parameters that need to be determined in the mechanical design. The relative displacement x of the mechanism is the only independent variable in the formula. Therefore, the function of the output force of the SNEMA with respect to the displacement x can be articulated as

$$\mathrm{F}(x) = k \cdot (2L\cos\theta_0 - x) - \frac{2kL\sin\theta_0(2L\cos\theta_0 - x)}{\sqrt{4L^2 - (2L\cos\theta_0 - x)^2}}. \tag{7}$$

The equivalent force stiffness of the SNEMA K_{eq} is defined as

$$\delta F_{out} = K_{eq} \cdot \delta x. \tag{8}$$

Therefore, K_{eq} can be derived as

$$K_{eq} = \mathrm{K}(x) = \frac{\delta F_{out}}{\delta x} = -k \cdot \left(1 - \frac{8L^3\sin\theta_0}{\left(4L^2 - \left(x - 2L\cos\theta_0\right)^2\right)^{\frac{3}{2}}}\right). \tag{9}$$

It is evident that the equivalent stiffness of the SNEMA presents a nonlinear relationship. The nonlinearity is primarily attributed to the term $\left(1 - \frac{8L^3\sin\theta_0}{\left(4L^2 - (x - 2L\cos\theta_0)^2\right)^{\frac{3}{2}}}\right)$ in Eq. (9), which arises from the distinctive geometric properties of the diamond. Additionally, it is noted that the equivalent stiffness K_{eq} is directly proportional to the stiffness of the elastic elements k incorporated within the SNEMA.

Fig. 3 shows the nonlinear profile of F_{out} and K_{eq} with respect to x. It can be observed that the force and stiffness curves can be divided into two distinct regions at the critical point x_m. The critical point x_m represents a critical shift in the stiffness characteristics of the SNEMA, distinguishing between the softening and hardening stiffness behavior. When the relative displacement x of the mechanism is less than x_m, it exhibits a softening stiffness behavior, characterized by a decrease in force stiffness as x increases, ultimately reaching a force stiffness of zero. When the relative displacement x surpasses x_m, the SNEMA exhibits a negative hardening stiffness behavior. In this region, the output force F_{out} decreases until it reaches zero.

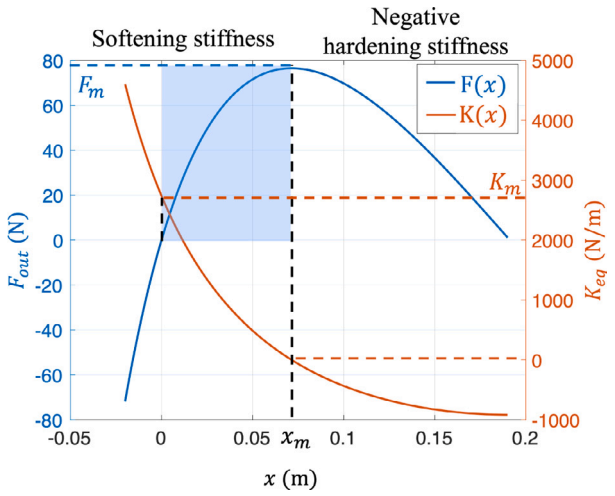

Fig. 3. The output force F_{out} and equivalent stiffness K_{eq} performance of the SNEMA with $L = 0.15$ m, $\theta_0 = 0.28\ \pi$, $k = 4000$ N/m. The specified working range, $x \in [0, x_m]$, is highlighted with blue shading.

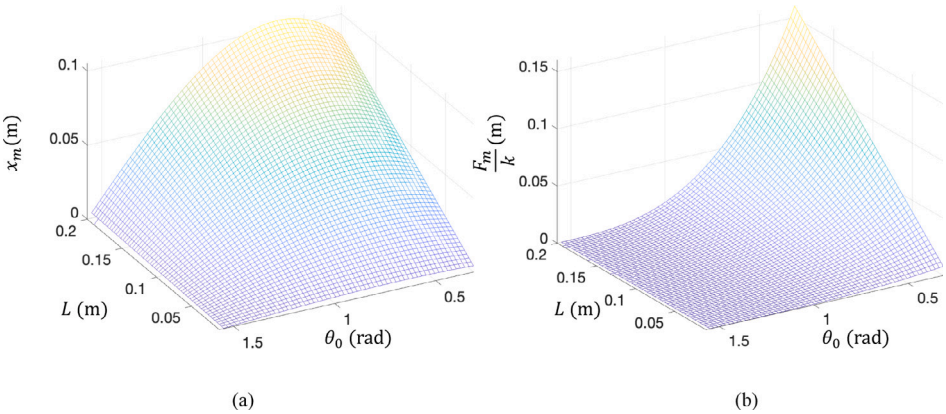

(a) (b)

Fig. 4. The variation of x_m and F_m/k for varying link length L and initial mechanism angle θ_0.

Given the design imperatives, it is essential to achieve a softening stiffness profile to ensure a compact overall structure, facilitates precise force control, and guarantees safety during human–robot interaction. Moreover, the SNEMA is designed to provide forward force to assist humans in locomotion. To achieve these objectives, our focus will be on optimizing the force and stiffness characteristics of the SNEMA within the range $x \in [0, x_m]$. As indicated by the blue shading in Fig. 3, the SNEMA exhibits a softening stiffness behavior and generates a positive forward force. It is observed that the two key points, the initial point ($x = 0$) and the critical point ($x = x_m$), can effectively depict the output characteristics of the SNEMA. At the critical point, the mechanism reaches the maximum compression and generates the maximum output force (F_m), accompanied by a zero-equivalent stiffness. The point x_m can be obtained by solving the root of the K_{eq}, which is

$$x_m = 2L\left(\cos\theta_0 - \sqrt{1 - (\sin\theta_0)^{\frac{2}{3}}}\right). \tag{10}$$

Therefore, the maximum force F_m can be obtained as

$$F_m = \mathrm{F}(x_m) = 2kL\left(1 - (\sin\theta_0)^{\frac{2}{3}}\right)^{\frac{3}{2}}. \tag{11}$$

Eqs. (10) and (11) indicate that the stroke length (x_m) and the maximum output force (F_m) of the mechanism are directly proportional to the link length (L) and the spring stiffness (k), and exhibit a nonlinear relationship with the initial mechanism angle (θ_0), as shown in Fig. 4.

In the initial state, the SNEMA generates a zero output force, accompanied by the maximum equivalent stiffness (K_m), which can be obtained by substituting $x = 0$ into Eq. (9)

$$K_m = \mathrm{K}(0) = \frac{k}{\tan^2 \theta_0}. \tag{12}$$

Eq. (12) indicates that the maximum equivalent stiffness within the defined range of motion is only influenced by the initial mechanism angle θ_0. It is worth noting that an increase in the θ_0 results in a reduction of the maximum equivalent stiffness K_m.

The kinetic principle and stiffness modeling of the proposed diamond-shaped SNEMA examine the effects of mechanism parameters on its performance characteristics, offering critical insights for parameter selection, adjustable stiffness establishment, and prototype design.

3. Adjustable stiffness profile and configuration selection

3.1. Adjustable stiffness profile

According to the stiffness modeling, the displacement–force relationship and the nonlinear-stiffness performance of the SNEMA are determined by the parameters k, θ_0, and L, as shown in Eqs. (7) and (9). To achieve adjustable nonlinear-stiffness profile, changing the related mechanism parameters can change the output force and stiffness characteristics of the SNEMA. Considering that changing the stiffness k of the linear spring means changing the type of spring, it is not feasible in practical applications. In this subsection, the effect of changing θ_0 and L on the output force and the stiffness profile will be analyzed to achieve the adjustable output characteristics of the SNEMA.

Fig. 5(a) illustrates the impact of varying the initial mechanism angle θ_0 on the output performance of the SNEMA. The right subplot of Fig. 5(a) shows the mechanism output curves associated with three distinct values of θ_0. It is evident from the figure that there is an inverse correlation between θ_0 and both the maximum output force F_m and the degree of nonlinearity of the stiffness profile. This indicates that as θ_0 increases, the range of output force decreases, accompanied by a decrease in maximum stiffness K_m and a decrease in the nonlinearity of the stiffness profile. When θ_0 changes from 0.26π to 0.30π, the maximum output force F_m increases by 73.1%. Similarly, Fig. 5(b) shows the impact of varying the length of link L on the output performance of the proposed mechanism. The right subplot of Fig. 5(b) shows the output curves of the mechanism associated with three different values of L. Unlike the variation of θ_0, L is directly proportional to the maximum output force and the critical point x_m, while showing an inverse correlation with the degree of nonlinearity of the stiffness profile.

Comparing the two adjustment principles, it can be seen that decreasing the initial mechanism angle θ_0 by 13.3% leads to a 73.1% increase in the range of the output force, with the critical point x_m increasing from 0.0674 m to 0.0746 m. This results in a modest stroke variation increase by only 10.7%. This observation demonstrates that modifying the initial angle can amplify the output force capability of the SNEMA, while ensuring that the stroke remains relatively stable. Conversely, adjusting the link length results in proportional increases in the stroke range and the output force range. This approach significantly increases the spatial occupancy of the mechanism. In addition, implementing changes to the link length is complex to realize in the mechanical design. Therefore, adjusting the initial angle of the mechanism is a better option to increase the reconfigurability of the proposed SNEMA without significantly altering its workspace. This reconfigurability empowers the SNEMA to flexibly accommodate a range of working conditions and achieve specialized task performance.

3.2. Configuration parameter selection

As discussed in Section 3.1, the proposed SNEMA can alter the characteristics of the output force and stiffness by adjusting the initial angle θ_0. This subsection aims to showcase a case study that elucidates the calculation process for identifying the optimal mechanism configuration for a specific application scenario. These calculations will help to determine the parameters of the mechanism and serve as guidance for the prototype design process.

The criterion for determining the range of the SNEMA's configurations is to align the force profiles with the required output force range. For individuals with varying weights or diverse load-carriage scenarios, it is essential to provide appropriate forward force to match optimal assistance. Prior research findings indicate that forward assistance with a magnitude equivalent to approximately 8% of human body weight can significantly reduce the walking metabolic rate by 44% [11]. This crucial insight serves as a benchmark for defining the output force characteristics of the SNEMA. Considering the typical body weight of adults, ranging from 50 kg to 80 kg, and the maximum additional load of 30 kg, it is reasonable to approximate the ideal assistance force within 40 N to 88 N.

To maintain a compact design that harmonizes with the overall structural dimensions of the mechanism and its application platform, the link length L and the stiffness of the linear spring k are predetermined as 0.15 m and 4000 N/m, respectively. Although θ_0 can be continuously adjusted to generate continuously changing force and stiffness profiles, in order to facilitate adjustment in practical applications, the range of output force is divided into three distinct scenarios: low (40–56 N), medium (56–72 N), and high (72–88 N) output force. Three appropriate configuration θ_0 values will be calculated to meet the requirements of the output force within each designated range.

To guarantee the mechanism delivers sufficient bandwidth and maintains robust tracking performance for the intended range of assistance, the maximum output force at zero stiffness of each configuration should marginally exceed the highest required output force. This strategy involves setting F_m to be 110% of the maximum required force to obtain a preliminary value of θ_0. Specifically,

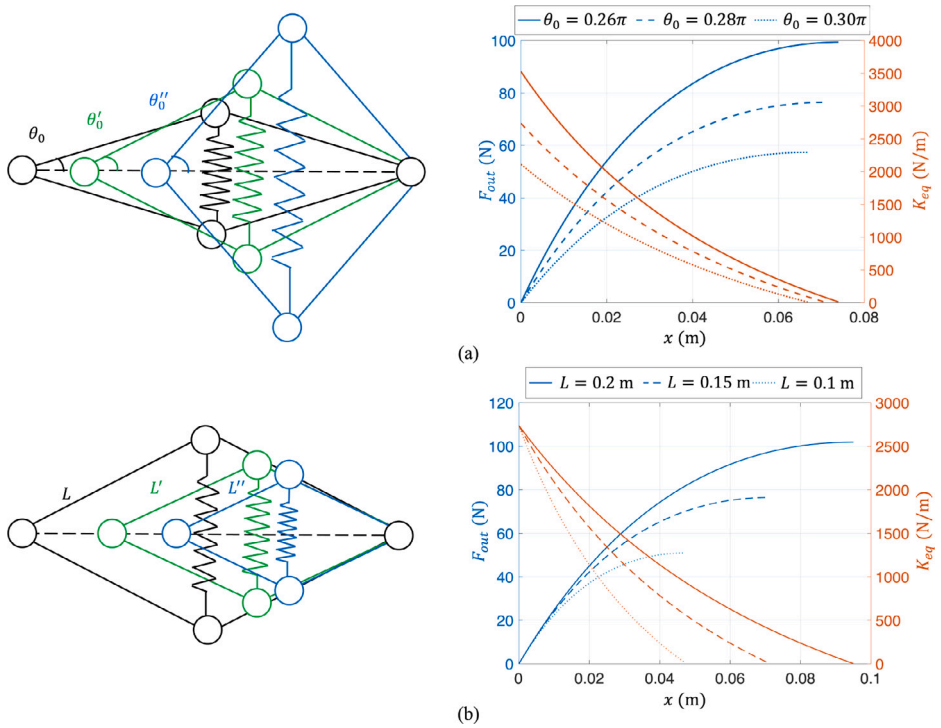

Fig. 5. The principle of adjustable stiffness profile. (a) Schematic diagram of the adjustment of the initial mechanism angle θ_0 and the force and stiffness performance under different θ_0 with $L = 0.15$ m and $k = 4000$ N/m. (b) Schematic diagram of the adjustment of the length of the link L and the force and stiffness performance under different L with $\theta_0 = 0.28\pi$ and $k = 4000$ N/m.

for the high output force working condition, corresponding to the required maximum output force of 88 N, F_m is set to be 96.6 N. According to stiffness modeling, as shown in Eq. (11), the value of θ_0 can be solved to be equal to 0.8239 rad, which can be approximated as 0.26π rad. In this configuration, the critical point x_m and the maximum stiffness K_m are 0.0746 m and 3527.4 N/m, respectively. For the medium output situation, F_m is designated as 79.2 N for the same reason. In this case, θ_0 is solved as 0.8715 rad, which is rounded to 0.28π rad. For the low output force range, F_m is set to 61.6 N, leading to a rounded value θ_0 of approximately 0.30π rad. The output force and equivalent stiffness curves of the SNEMA under three distinct configurations ($\theta_0 = \{0.26\pi, 0.28\pi, 0.30\pi\}$) are illustrated in Fig. 6. The utilization of three different θ_0 parameters guarantees the mechanism's output force within the range from 40 N to 88 N, facilitating the adaptability to different working conditions.

3.3. Stiffness model validation by simulation

Based on the stiffness modeling and adjustable stiffness analysis, a simulation was performed to validate the stiffness modeling and the force characteristics of the SNEMA. The conceptual model of SNEMA was established in Adams 2020 software, and force performance was simulated under three different initial mechanism angles: 0.26π, 0.28π, and 0.30π. Fig. 6 shows the results of the comparison between simulation and theoretical calculation. For the three different θ_0 from 0.26π to 0.30π, the root-mean-square (RMS) errors are 0.2284 N, 0.1795 N, and 0.1436 N, respectively; the maximum absolute errors are 0.3984 N, 0.2972 N, and 0.2255 N, respectively. The errors may be caused by the friction in the rotation joints between the links during motion. However, the discrepancies are within the acceptable range, and the agreement between the simulated output force curve and the theoretically calculated curve provides preliminary validation for the desired softening nonlinear stiffness of the proposed SNEMA. Moreover, the variation in output characteristics across different initial mechanism angles confirms the stiffness adjustability of the proposed SNEMA.

4. The realization of the SNEMA

The preceding sections have introduced and analyzed the stiffness model and variable stiffness principle of the SNEMA, establishing a theoretical foundation. However, directly applying these concepts to the SNEMA's practical mechanical implementation poses certain challenges. This section outlines the process for realizing the proposed SNEMA, bridging the gap between conceptual design and physical realization.

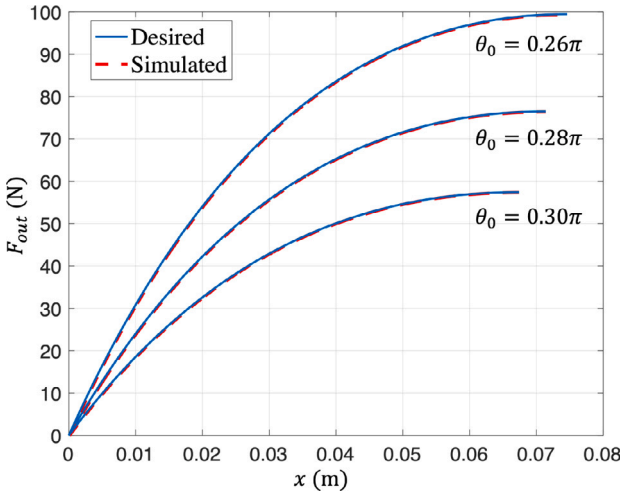

Fig. 6. Results of theoretical calculation and simulated output force under three selected initial mechanism angles θ_0.

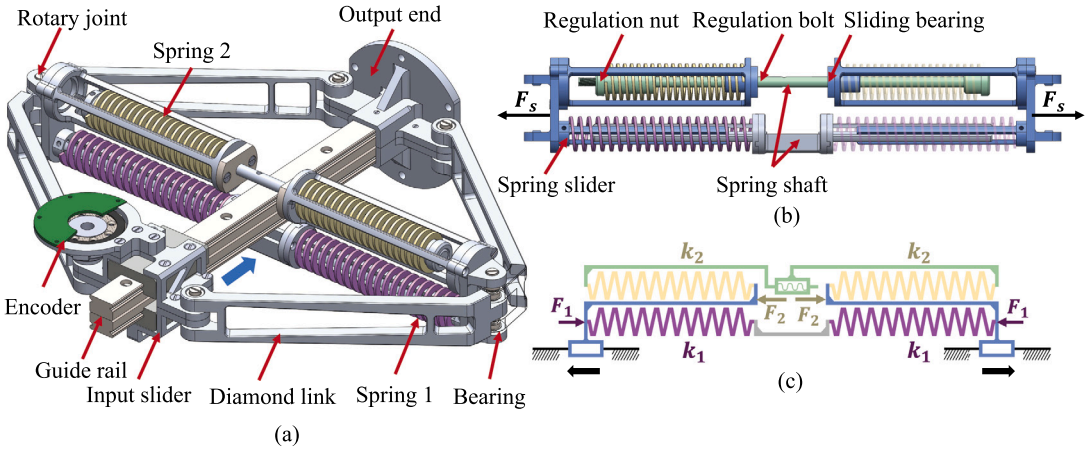

Fig. 7. Mechanical design of the SNEMA. (a) Overview of the 3D model of the SNEMA. (b) The 3D model of the antagonistic-spring regulation mechanism. To better illustrate the details, the springs on the right are rendered transparent in the diagram. Different colors are used to distinguish the relative translation relationships within the mechanism. Parts highlighted in blue move in relative translation with respect to the parts colored in green and gray, respectively. F_s represents the external force to counterbalance the spring tensions. Its direction is opposite to the net force generated by the two antagonistic springs. (c) Mechanism schematic diagram of the antagonistic-spring regulation mechanism. F_1 and F_2 indicate the external force components that balance the elastic forces of spring 1 and spring 2, respectively. (For interpretation of the references to color in this figure legend, the reader is referred to the web version of this article.)

In the conceptual design, as the mechanism compresses, the length of the VD increases, implying the need for a tension spring in the SNEMA. In practical mechanical design, tension springs typically possess a certain level of initial tension and are limited to stretching, which may reduce the working space of the SNEMA and can lead to a sudden change of the stiffness at the initial position. Moreover, to achieve a variable stiffness profile, the initial equilibrium angle of the mechanism θ_0 should be adjusted according to the different task situations. However, achieving equilibrium at different mechanism angles is impractical with a single linear spring. To overcome these issues, an antagonistic-spring regulation mechanism employing two types of compression springs is proposed to mimic the function of the tension spring in the conceptual design. This regulation mechanism is designed to fine-tune the pre-compression level of one spring to change the initial mechanism angle, thus altering the output stiffness characteristics of the SNEMA.

4.1. Physical implementation

As illustrated in Fig. 7(a), the 3D model of the proposed SNEMA is built to be mirror-symmetrical based on the analysis of the conceptual model. The physical implementation of the SNEMA mainly consists of two parts: the diamond-shaped framework and the antagonistic-spring regulation mechanism. The diamond-shaped framework consists of four links of equal length and two sliders.

Each diamond link is connected to the vertexes of the diamond-shaped framework via a rotary joint. One end is connected to the antagonistic-spring regulation mechanism in the VD, and the other end is connected to the input slider and the output end along the HD. The input slider is driven to translate along the guide rail, while the output slider is linked to the human side. Therefore, the geometric characteristics of the proposed prototype is equivalent to the conceptual diamond SNEMA analyzed in Section 2. The mechanism angle θ of the SNEMA is measured by an absolute encoder (MB039, RLS, Komenda, Slovenia) with a resolution of 17 bits. The relative displacement x between the input and output ends can be uniquely determined by θ, denoted by

$$x = 2L(\cos\theta_0 - \cos\theta). \tag{13}$$

Fig. 7(b) shows the 3D model and the schematic diagram of the antagonistic-spring regulation mechanism. The spring slider, colored blue, is designed to translate along the upper and lower spring shafts, which are colored green and gray, respectively. The hollow design of the shafts and the usage of sliding bearings are designed to reduce friction during the translational motion. Two kinds of compression springs are assembled on the spring slider with pretension along the VD direction of the SNEMA, with each type of compression spring comprising two identical springs connected in series. The compression springs are both constrained at one end by the spring slider and at the other by the end of the respective spring shaft, but they are in different arrangements. The outer end surface of spring 1 connects to the spring slider, while for spring 2, it is the inner end surface that is connected. This unique arrangement causes the springs to exert antagonistic forces on the spring slider, as depicted by F_1 and F_2 in the mechanism schematic diagram. When the SNEMA is not subjected to external forces, spring 1 generates an antagonistic force, F_1, corresponding to the pre-compression force of spring 2 to maintain balance. The upper spring shaft consists of a long regulation bolt and a regulation nut. By rotating the regulation bolt, the pre-compression amount of spring 2 can be modified, resulting in a change in the elastic force F_2 of spring 2. The change of F_2 will induce translation of the spring slider to adjust the compression amount of spring 1 accordingly, allowing the elastic mechanism to maintain equilibrium at a new mechanism angle. Hence, the regulation mechanism can modify the initial mechanism angle θ_0 to customize the output force profile.

When the mechanism is relatively compressed, the spring slider moves outward, as indicated by the black arrow in the schematic diagram. This movement leads to the relaxation of spring 1 and further compression of spring 2, resulting in a larger F_2 compared to F_1. Consequently, the net force of these two springs acts inward, effectively simulating the behavior of a tension spring. The behavior of the two antagonistic springs ensures the congruence of the mechanical properties of the physical implementation with the conceptual design. F_s denotes the resultant elastic force of the mechanism, which is equivalent to the F_s defined in Eq. (4) in the conceptual design. In the prototype of the SNEMA, as shown in Fig. 7(b), F_s is the resultant elastic force on VD, which can be expressed as

$$F_s = F_2 - (-F_1) = \frac{1}{2}(k_1 + k_2)(l_v - l_{v0}), \tag{14}$$

where $(l_v - l_{v0})$ represents the change in length of the VD; the factor $\frac{1}{2}$ accounts for the fact that the two identical compression springs are connected in series, resulting in each spring undergoing half of the change in diagonal length. Comparing Eq. (14) with Eq. (4), it can be seen that the overall linear spring stiffness k of the designed SNEMA prototype can be equivalently expressed as half of the sum of k_1 and k_2, denoted by

$$k = \frac{1}{2}(k_1 + k_2). \tag{15}$$

The proposed mechanical design of the SNEMA takes advantage of the antagonistic characteristics of the two compression springs and the capacity for adjustable pre-compression to achieve the equilibrium of the mechanism at different angles.

4.2. Constraints of spring selection

To guarantee that the compression springs operate linearly within the specified working range of the SNEMA, it is essential to avoid spring relaxation and solid height compression. Therefore, this section details the modeling of two springs and the selection of appropriate spring parameters. These parameters are chosen based on equality and inequality constraints that consider the size of the SNEMA prototype and the working characteristics of the antagonistic springs. To effectively model the two compression springs, three critical parameters are typically used: the stiffness (k_1, k_2), the rest length (l_{10}, l_{20}), and the maximum compression ratio (C). To ensure the springs operate within the linear stiffness range, it is essential to adhere to certain constraints regarding the current spring length (l_1, l_2) and the stiffness, expressed as

$$(1 - C)\, l_{10} \le l_1 \le l_{10}, \quad (1 - C)\, l_{20} \le l_2 \le l_{20}; \tag{16}$$

$$k_1 + k_2 = 2k, \tag{17}$$

where k is the equivalent stiffness of the linear spring in conceptual SNEMA. The constraint (17) is established based on the relationship derived from Eq. (15).

Generally, for varying configurations of the SNEMA $\theta_0 \in [\theta_{0min}, \theta_{0max}]$, as well as the corresponding working ranges $x \in [x_{min}, x_{max}]$ for each configuration, the lengths l_1 and l_2 of compression springs Spring 1 and Spring 2 must comply with the inequality constraint (16).

Given the geometric characteristics of the diamond mechanism and the structural dimensions of the prototype, the relationship between the current length of springs and the current mechanism angle θ can be articulated as

$$l_1 = \mathrm{L}_1(\theta) = L\sin\theta - 0.5\delta, \tag{18}$$

$$l_2 = \mathrm{L}_2(\theta_0, \theta) = l_{20} - \underbrace{\frac{k_1\left(l_{10} - \mathrm{L}_1(\theta_0)\right)}{k_2}}_{\Delta l_{pre}} - \underbrace{L(\sin\theta - \sin\theta_0)}_{\Delta l_{com}}, \tag{19}$$

where L indicates the length of the diamond link and θ_0 represents the configuration of the SNEMA. δ represents the length occupied by the prototype components along the axis of spring 1. l_1 depends solely on the current mechanism angle θ and is independent of the configuration θ_0. Δl_{pre} is the pre-compression amount of spring 2 in the configuration θ_0, and Δl_{com} represents the change in the length of spring 2 introduced by the relative motion of the SNEMA's input and output ends. Substituting Eq. (18) into Eq. (19) and rearranging it, we can further get

$$l_2 = \mathrm{L}_2(\theta_0, \theta) = (\frac{k_1}{k_2} + 1)L\sin\theta_0 - L\sin\theta + l_{20} - \frac{k_1}{k_2}l_{10} - \frac{k_1\delta}{2k_2}. \tag{20}$$

Analysis of $\mathrm{L}_1(\theta)$ and $\mathrm{L}_2(\theta_0, \theta)$ reveals that $\mathrm{L}_1(\theta)$ monotonically increases with θ, while $\mathrm{L}_2(\theta_0, \theta)$ monotonically increases with θ_0 and decrease with θ. Then the maximum and minimum lengths of the two antagonistic springs within a specific mechanism configuration and working range can be determined. By substituting these extreme conditions into inequality (16) and (17), a valid spring parameter constraint can be derived as

$$\mathrm{L}_1(\theta_{min}) \geq (1 - C)\, l_{10}, \quad \mathrm{L}_1(\theta_{max}) \leq l_{10}; \tag{21}$$

$$\mathrm{L}_2(\theta_{0min}, \theta_{max}) \geq (1 - C)\, l_{20}, \quad \mathrm{L}_2(\theta_{0max}, \theta_{min}) \leq l_{20}; \tag{22}$$

$$k_1 + k_2 = 2k. \tag{23}$$

Specifically, for the proposed SNEMA prototype, specific parameters are given as follows: $k = 4000$ N/m, $L = 0.15$ m, $\theta_0 \in \{0.26\pi, 0.28\pi, 0.30\pi\}$, $x \in [0, x_m]$, $\delta = 0.015$ m, and $C = 0.5$. Given these settings, the constraints can be further simplified. Moreover, in terms of stiffness distribution between the two springs, the stiffness ratio k_1/k_2 is set to less than 0.5 to minimize the stroke required for the regulation nut. Based on these constraints and the standard spring specifications, the stiffness of spring 1 and spring 2 that meet the requirements are determined to be 2400 N/m and 5600 N/m, respectively. The respective rest lengths are selected as 0.150 m and 0.100 m.

Following a bench test to measure the stiffness of the springs, the actual stiffness and stiffness linearity of the chosen compression springs were evaluated. The results indicated that the selected springs conformed well to Hooke's law, with measured actual stiffness values of 2400 N/m and 5800 N/m. Under this selection, the equivalent linear spring stiffness is 4100 N/m, with an acceptable selection error of 2.5%. Additionally, the stiffness and length of the selected compression springs also meet the previously mentioned constraints.

4.3. Stiffness model validation by bench test

A quasi-static test was conducted on the bench test system to verify the applicability of the stiffness model derived during conceptual design to the SNEMA prototype designed above. The force–displacement relationship of the SNEMA was measured under three different initial mechanism angles ($\theta_0 = \{0.26\pi, 0.28\pi, 0.30\pi\}$). Three sets of repeated measurements were carried out for each configuration. The results of the measurement were depicted in Fig. 8. The RMS errors of each configuration ($\theta_0 = \{0.26\pi, 0.28\pi, 0.30\pi\}$) were 0.9955 ± 0.1075 N (mean ± standard error), 0.8082 ± 0.0630 N, and 1.3690 ± 0.0347 N, respectively. Considering the assembly errors in manufacturing and friction between the mechanical components, the relatively larger errors in the prototype experiments compared to the simulation tests are within a reasonable and acceptable range. Overall, the alignment between the measured data from multiple experiments and the theoretical calculation results indicates the accuracy of the kinematic and stiffness model developed in Section 2.

5. Force control strategy and force tracking, interaction performance in varied stiffness configurations

In this section, the force control strategy will be proposed to achieve precise and robust output force control of the SNEMA. The force tracking and the interaction performances while varying the stiffness configurations of the SNEMA prototype are evaluated through experiments. The comprehensive experiments aim to showcase the advantages of the proposed SNEMA in human–robot interaction force control.

5.1. Force control strategy

The input end of the SNEMA is required to be driven by a generalized translational actuator, as shown in Fig. 9(a). The generalized actuator typically represents the robot to which the input end of the SNEMA is connected. In the application platform assumed in this paper, the actuator is regarded as the torso of the Centaur robot, as shown in Fig. 1(b). By employing the proposed kinematic model of the SNEMA, the output force control is transformed into the relative position control.

A PD controller with a position outer-loop and a velocity inner-loop is proposed to achieve the accurate and robust force control of the SNEMA, as shown in Fig. 9(b). Since the control of the output force of the SNEMA involves regulating the relative position of the input and output ends, the desired force F_{ref} must first be converted into the desired position x_d in real-time. According to the kinematic model of the SNEMA, as depicted in Eq. (7), it is important to note that the relationship between F_{ref} and x_d is

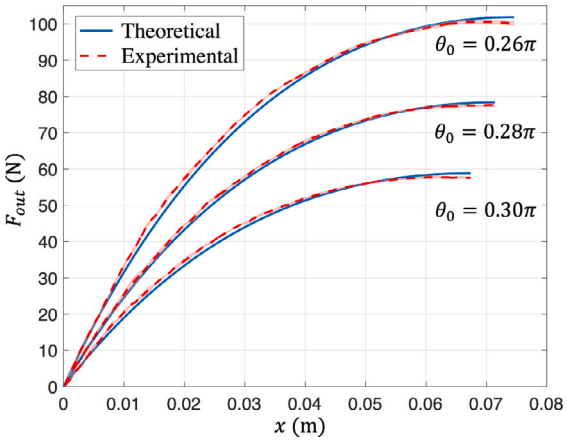

Fig. 8. Experimental results of the prototype model validation. The blue solid line and the red dashed line denote the theoretical results and the average experimental results, respectively. The red-shaded area represents the distribution of results from multiple trials.

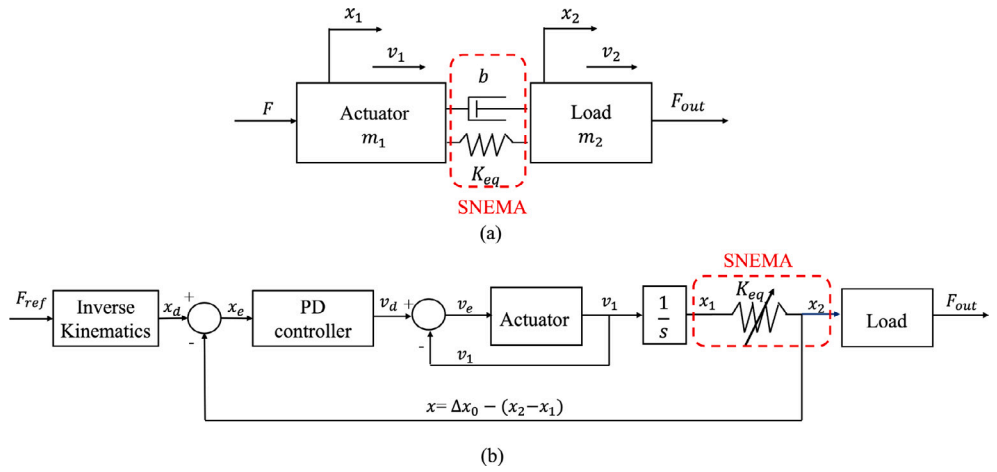

Fig. 9. Block diagram of the SNEMA and the force controller. (a) Schematic of the SNEMA with the actuator in translation direction. (b) The PD force controller with a relative position x outer loop and a velocity inner loop.

nonlinear. To resolve the issue, the Secant method [38] is employed to obtain the inverse numerical kinematics, and the iteration formula can be expressed as

$$x_{k+1} = x_k - \frac{\left(\mathrm{F}(x_k) - F_{ref}\right)\left(x_k - x_{k-1}\right)}{\mathrm{F}(x_k) - \mathrm{F}(x_{k-1})}, \quad k = 1, 2, 3, 4, \ldots \tag{24}$$

where x_k is the k_{th} iteration point, $\mathrm{F}(x_k)$ is the function to calculate the output force (as described in Eq. (7)), and the iteration procedure starts with two initial points x_1 and x_0.

The designed PD controller is the outer-loop controller and generates the desired translation velocity command v_d to the actuator according to the position tracking error x_e. The PD controller is designed as

$$v_d = \left(K_p + K_d s\right) x_e, \tag{25}$$

where s represents the Laplace operator; K_p and K_d are the control parameters of the PD controller, respectively. The velocity command v_d is subsequently transmitted to the actuator. The outer-loop PD controller tracks the desired position x_d through the inherent velocity tracking ability of the actuator.

5.2. Experimental setup

A prototype of the proposed SNEMA was developed, and a bench test system was built to verify the performance of stiffness modeling and force control, as shown in Fig. 10. An electric motor (GO-M8010-6, Unitree, China) paired with a ball screw was used to form a translational actuator as the input actuator for the SNEMA. The ball screw slider was responsible for driving the input

Table 1
Specification of the SNEMA prototype.

Specification parameters	Values	Unit
Weight	1.33	kg
Length of link (L)	0.15	m
Equivalent stiffness of linear spring (k)	4100	N/m
Stiffness of spring 1 (k_1)	2400	N/m
Stiffness of spring 2 (k_2)	5800	N/m
Rest length of spring 1 (l_{10})	0.150	m
Rest length of spring 2 (l_{20})	0.100	m
Initial mechanism angle (θ_0)	$\{0.26\pi, 0.28\pi, 0.30\pi\}$	rad
Peak output force (F_m)	{101.89, 78.38, 58.83}	N
Maximum equivalent stiffness (K_m)	{3615.5, 2806.0, 2164.2}	N/m
PD controller parameters ($\{K_p, K_d\}$)	{18.6, 8.0}	–

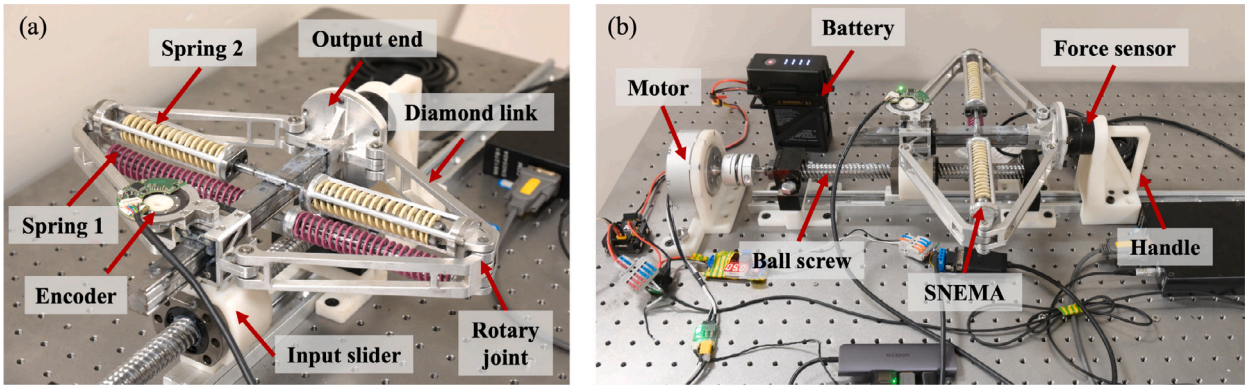

Fig. 10. Experiment setups of the bench test. (a) The prototype of the SNEMA. (b) The bench test system. The bench test system consists of a translational actuator, the SNEMA prototype, a force sensor, and a handle. The translational actuator comprises a battery, motor, and ball screw.

end to generate force at the output end. The output end was connected to a six-axis force sensor (M3813D, SRI, China) to measure the actual output force of the SNEMA. An interaction handle was also connected to the output end of the SNEMA, which can slide on the rail to access the dynamic performance of the force control. A laptop computer based on Linux OS was employed to run the controller codes and collect data from the absolute encoder and the force sensor, both operating at a frequency of 120 Hz. The key specification parameters of the SNEMA prototype are listed in Table 1. Acknowledging the possibility of variance between the actual stiffness of the physical spring and its theoretical nominal value, the calibrated equivalent stiffness of the linear spring k is confirmed to be 4100 N/m in the prototype.

5.3. Force tracking performance

Due to the softening nonlinear-stiffness profile, the equivalent stiffness of the SNEMA varies with different output forces, resulting in varying tracking performance on the reference force. The softening stiffness profile of the mechanism can be categorized into two regions: the high stiffness range and the low stiffness range. The boundary between these regions is set at 50% of the maximum stiffness K_m, with 0% K_m to 50% K_m representing the low stiffness area and 50% K_m to 100% K_m denoting the high stiffness area.

To evaluate the performance of the output force control with the proposed force controller, the step response and sinusoidal tracking experiments were conducted. The force tracking results of the step response and sinusoidal trajectory for different stiffness ranges will be compared and analyzed to demonstrate the advantages of the softening stiffness behavior.

5.3.1. Step response

In the step response experiment, the reference values for the step response were set to force values in different stiffness ranges. These reference values were specifically determined based on the maximum equivalent stiffness of the SNEMA under the particular configuration. Three different reference forces were selected under each configuration, which corresponded to 75%, 50%, and 25% of the maximum stiffness K_m, respectively.

Fig. 11(a)–(c) shows the step response for force control under three configurations of the mechanism, i.e., $\theta_0 = \{0.26\pi, 0.28\pi, 0.30\pi\}$. In all step experiments, the proposed controller demonstrates efficient force control results, rapidly compressing the SNEMA to achieve the desired output force. The rise time is less than 0.5 s, and as the stiffness decreases, the overshoot is also getting smaller. Fig. 11(d) and (e) present the mean and standard deviation of the force control RMS error and position control RMS error across multiple experiments. As stiffness decreases, there is a noticeable degradation in the tracking performance of the elastic mechanism, leading to a gradual increase in position control error. However, the low stiffness improves the force control resolution,

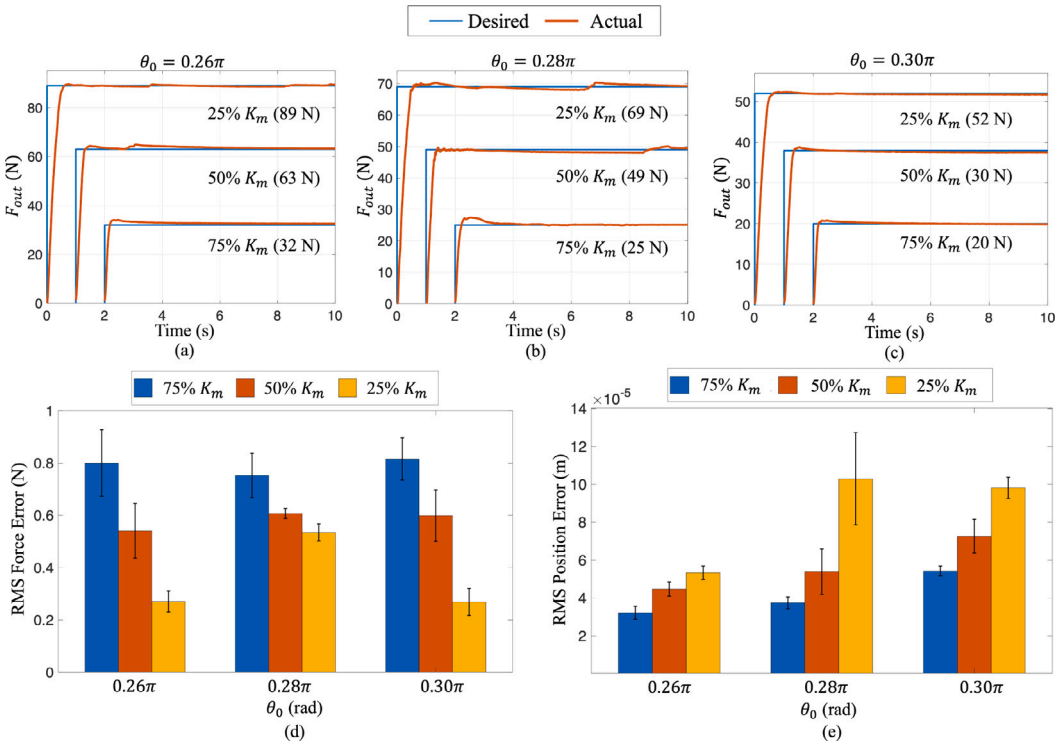

Fig. 11. Experimental results of the step response for force control. (a–c) Step force response diagrams corresponding to different stiffness for one single run. The left-to-right arrangement corresponds to the different configurations of 0.26π, 0.28π, and 0.30π, respectively; the top-to-bottom sequence within each figure represents force reference values with different stiffness of 25% K_m, 50% K_m, and 75% K_m, respectively. (d) The RMS force errors (mean values and standard deviation) of the step response for multiple repeated experiments. (e) The RMS position errors (mean values and standard deviation) of the step response for multiple repeated experiments.

Table 2
Control performance for step response.

θ_0	RMS error (N)		
	75% K_m	50% K_m	25% K_m
0.26π	0.7999 ± 0.1270	0.5408 ± 0.1043	0.2704 ± 0.0399
0.28π	0.7524 ± 0.0846	0.6072 ± 0.0192	0.5346 ± 0.0330
0.30π	0.8153 ± 0.0807	0.5989 ± 0.0985	0.2688 ± 0.0518

resulting in smaller force control errors even in the presence of high position control errors. Table 2 lists the step force control RMS errors under different initial mechanism angles and different stiffness, and all the average RMS errors are below 1% of the reference values. The results demonstrate that for reference force trajectories with small dynamic changes, low stiffness can improve force control accuracy by improving the resolution of force control. The softening stiffness behavior leverages this feature to achieve higher precision force control within the target output force range.

5.3.2. Sinusoidal tracking

For dynamic force tracking performance, a sinusoidal curve with an amplitude of 5 N is selected as the reference trajectory. Considering that the period of aiding force profile should be consistent with the human gait cycle, the frequency of the sinusoidal force reference trajectory is set to 1 Hz (the gait cycle of normal human walking is approximately 1 s [39]). The reference sinusoidal force trajectory can be denoted by

$$F_{ref} = F_0 + 5\sin(2\pi t), \tag{26}$$

where F_0 is the offset of the reference sinusoidal force trajectory. By changing the value of F_0, the sinusoidal force tracking performance in different stiffness ranges can be analyzed and compared. It is important to note that as stiffness decreases, especially when it approaches zero, the dynamic performance of force tracking tends to deteriorate due to a reduction in system bandwidth. Therefore, we dedicated a zero stiffness area (0%–25% K_m) within the general low stiffness area to explore the tracking performance under dynamic tracking conditions. In this part, the sinusoidal tracking experiments were conducted separately for the high stiffness (50%–100% K_m), low stiffness (25%–50% K_m), and zero stiffness (0%–25% K_m) under different configurations of the SNEMA.

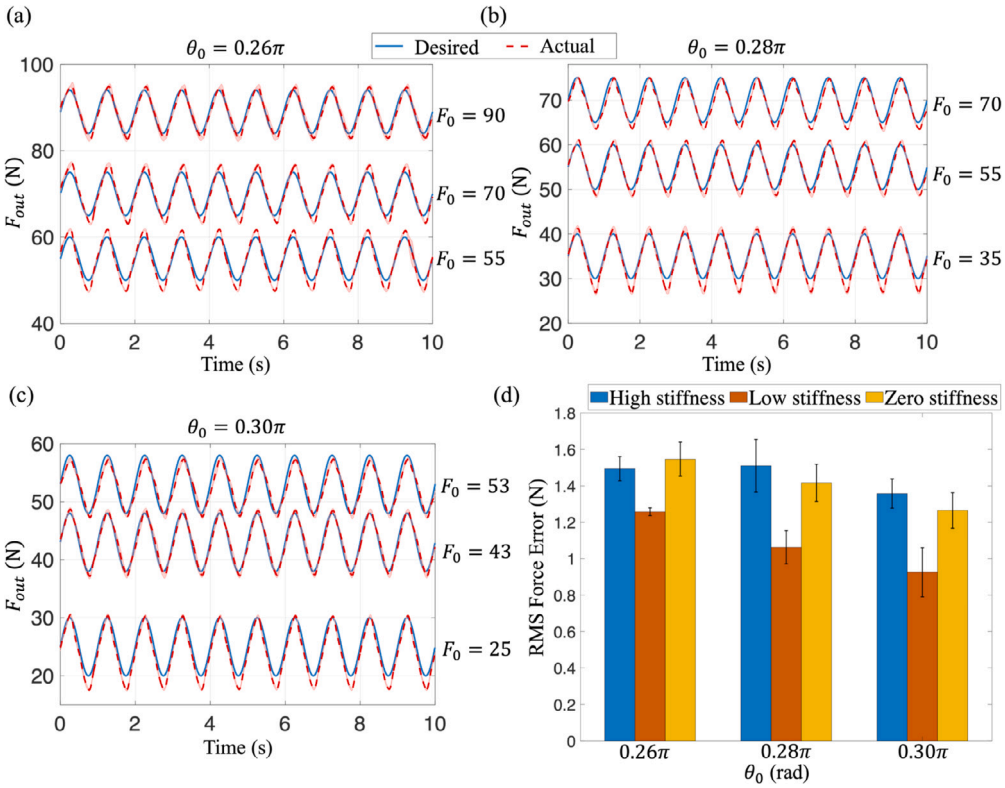

Fig. 12. Experimental results of the sinusoidal force tracking control. (a–c) Mean tracking values with standard deviations of the sinusoidal force tracking under different configurations. The blue line represents the desired sinusoidal trajectory, the red dashed line represents the average of the actual tracking trajectories in multiple experiments, and the red shading represents the standard deviation distribution. The top-to-bottom sequence within each figure represents force reference values with different stiffness of zero stiffness, low stiffness, and high stiffness, respectively. (d) The RMS force errors (mean values and standard deviations) of the sinusoidal tracking for multiple repeated experiments. (For interpretation of the references to color in this figure legend, the reader is referred to the web version of this article.)

Fig. 12(a)–(c) shows the sinusoidal tracking results and the standard deviation distribution under three configurations of the SNEMA. Each tracking trajectory can closely match the desired reference sinusoidal trajectory, demonstrating the good force tracking performance of the proposed PD controller and the SNEMA. However, due to the nonlinear softening stiffness behavior, there are still differences in the tracking performance of the same-shaped sinusoidal trajectory with different force offsets. Fig. 12(d) illustrates the distribution of the RMS errors in sinusoidal force tracking under different stiffness. It can be seen from the figure that the force tracking errors present a U-shaped trend as the stiffness decreases, which is consistent with the prior expectation. For the high stiffness condition, the actual force can track the phase change of the sinusoidal force trajectory quickly due to the high system bandwidth, but the actual tracking trajectory exhibits peak overshoot due to the poor force resolution associated with high stiffness. The low stiffness condition can better balance the trade-off between tracking performance and force resolution to achieve accurate dynamic force tracking. As stiffness continues to decrease and reaches the zero stiffness area, due to the insufficient bandwidth of the system in this situation, it is no longer possible to track the changes in sinusoidal force trajectory in time. An obvious hysteresis phenomenon can be seen in Fig. 12(a)–(c), and the tracking errors of the zero stiffness conditions become larger compared to the low stiffness conditions.

In order to quantitatively evaluate the tracking differences among different stiffness conditions, the gain and phase delay between the actual tracking trajectory and the desired trajectory were calculated for all conditions. Table 3 lists the RMS error, gain, and phase delay for various combinations of mechanism configurations and force offset values. In the low stiffness conditions, the RMS errors are 1.2576 ± 0.0214 N, 1.0624 ± 0.0913 N, and 0.9524 ± 0.1349 N for three configurations, respectively, all below 2% of the peak force values. Furthermore, the calculated gain and phase delay values align with the previous analysis. As the stiffness decreases, the gain of force tracking continues to decrease while the phase delay gradually increases. The combined effect of these trends results in optimal force dynamic tracking performance in the low stiffness area. The high stiffness and zero stiffness conditions lead to sub-optimal performance due to lower force resolution and reduced system bandwidth, respectively.

An inter-group comparison was also conducted in the experiment. For the sinusoidal reference trajectories with F_0 equal to 70 N and 55 N, the tracking performances are compared under two mechanism configurations ($\theta_0 = 0.26\pi, 0.28\pi$) to verify the conclusion further. The data in Table 3 reveals that for the desired trajectory of the sinusoidal force with $F_0 = 55$ N, the tracking RMS error is 1.4938 ± 0.0664 N when the initial mechanism angle is 0.26π. For the configuration of $\theta_0 = 0.28\pi$, the RMS error is 1.0624 ± 0.0913

Table 3
Control performance for sinusoidal tracking.

θ_0	Parameter	Tracking quality		
		High stiffness	Low stiffness	Zero stiffness
0.26π	F_0	55	70	90
	RMS error (N)	1.4938 ± 0.0664	1.2576 ± 0.0214	1.5466 ± 0.0933
	Gain	1.4122	1.3438	1.2203
	Phase delay (rad)	0.1879	0.2082	0.2476
0.28π	F_0	35	55	70
	RMS error (N)	1.5103 ± 0.1447	1.0624 ± 0.0913	1.4168 ± 0.1018
	Gain	1.4052	1.1246	1.1377
	Phase delay (rad)	0.1111	0.2008	0.2293
0.30π	F_0	25	43	53
	RMS error (N)	1.3579 ± 0.0805	0.9254 ± 0.1349	1.2650 ± 0.0974
	Gain	1.2602	1.1246	0.9936
	Phase delay (rad)	0.1154	0.1848	0.2613

N. In comparison with the high stiffness condition, the low stiffness force tracking error is reduced by 28.9%, the gain is reduced from 1.4122 to 1.1246, and the phase delay is increased from 0.1879 to 0.2008. For the sinusoidal desired trajectory with $F_0 = 70$ N, the tracking RMS error in low stiffness is 1.2576 ± 0.0214 N, and the tracking RMS error in zero stiffness is 1.4168 ± 0.1018 N. Compared with the low stiffness condition, the tracking error in the zero stiffness condition is increased by 12.7%, the gain decreases from 1.3438 to 1.1377, and the phase delay increases from 0.2082 to 0.2293.

The results above affirm that the proposed PD controller and the SNEMA exhibit the capability to accurately track a dynamic force trajectory with high fidelity at a specified frequency. For the softening nonlinear-stiffness elastic mechanism, adopting appropriate low stiffness in the target interaction force range can strike a better balance between force tracking performance and force control resolution, leading to more accurate output force control.

5.4. Interaction performance

The SNEMA is proposed to decouple the human–robot system by introducing elastic elements, aiming to enhance the interaction performance between the human and the robot. In scenarios involving human–robot assistance, predicting and modeling the motion of the output end (human body) can be challenging, often rendering it an unknown disturbance to the control of the input end of the mechanism. To evaluate the control performance of the proposed SNEMA on the output force during human–robot interaction, interaction experiments were conducted. These experiments specifically explore the ladder step response to the disturbance motion of the output end and the human–robot interaction safety under sudden collision at the output end.

5.4.1. Ladder step response

In the ladder step interaction experiment, the desired output force trajectory is configured as a ladder step, starting at 40 N within the first 10 s and then increasing to 50 N at a rate of 5 N/s over the next 12 s. Concurrently, the handle at the output end of the prototype (Fig. 10(b)) is manually moved by a human at a frequency of 0.5 Hz, following an approximately sinusoidal trajectory with an amplitude of 3 cm.

Fig. 13(a)–(c) show the output force of the SNEMA in the ladder step interaction experiment under three different configurations. The initial mechanism angles of the three figures from left to right are 0.26π, 0.28π, and 0.30π, respectively. The RMS errors of multiple experiments with three different configurations are 2.6543 ± 0.1919 N, 2.1214 ± 0.1820 N, and 1.3784 ± 0.1222 N, respectively. As the initial mechanism angle θ_0 becomes larger, the stiffness of the SNEMA corresponding to the same desired ladder step continues to decrease. Due to the larger force resolution of low stiffness, the change in the output force of the SNEMA is smaller when subjected to the same level of disturbance, resulting in a more accurate output force control, as shown in Fig. 13(c). It is notable that for a specific output force trajectory, choosing an appropriate mechanism configuration to match the stiffness with the output force can significantly reduce the force control error, which is the advantage of the proposed adjustable softening stiffness profile. The experimental results validate the capability of the proposed SNEMA to achieve precise force control in the presence of output disturbance, which also ensures that the proposed SNEMA and controller can effectively and precisely control the human–robot interaction force.

5.4.2. Collision experiments

Ensuring the safety of human–robot interaction is a critical consideration in the design of compliant elastic mechanisms. The collision experiment aims to test whether the proposed SNEMA and PD controller can maintain robust force control and ensure safe interaction in scenarios where the output end (the human) suddenly stops or experiences an unexpected collision during the human–robot interaction. In the collision experiment, the SNEMA, configured in different θ_0, was controlled to keep a constant output force of 50 N. Subsequently, the handle was rapidly pushed towards the input end direction and collided with a fixed baffle located approximately 2 cm away. This was designed to simulate a collision or an emergency stop of the human. The changes in the output force of the SNEMA were recorded for analysis.

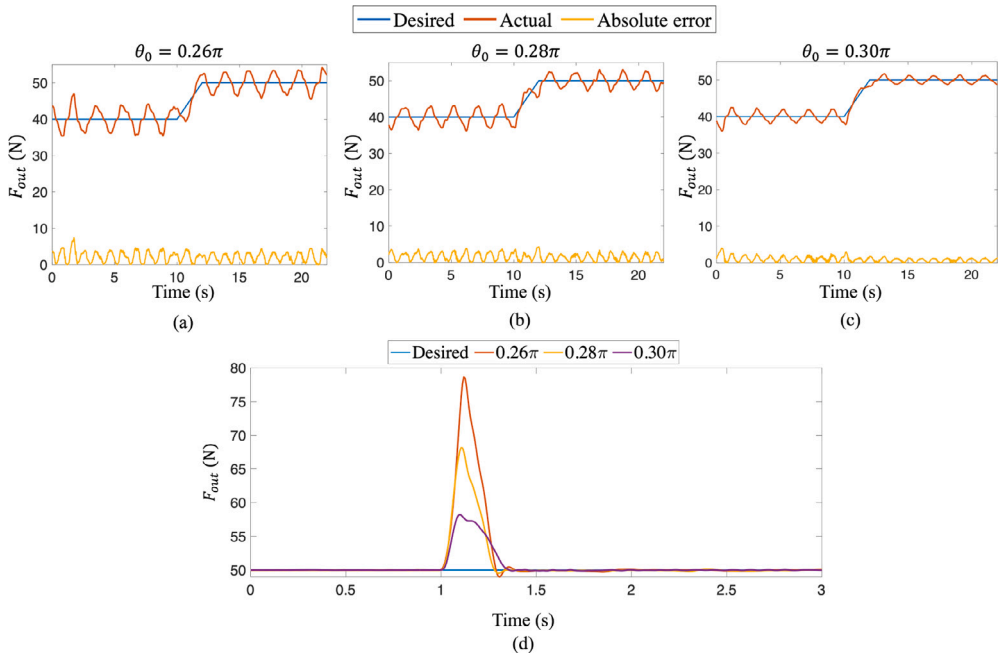

Fig. 13. Experimental results of interaction experiments. (a–c) The ladder step response diagram for one experiment under different configurations of the SNEMA. (d) The collision experimental results under different configurations of the SNEMA.

As depicted in Fig. 13(d), the output force experienced a sudden increase when the SNEMA was abruptly compressed. However, the proposed PD controller effectively restored the output force to the initially desired level within 0.4 s after the collision, with no instances of control failure observed across all three cases. Nevertheless, the peak forces observed post-collision varied significantly with different stiffness levels, which are 78.6 N ($\theta_0 = 0.26\pi$), 68.2 N ($\theta_0 = 0.28\pi$), and 58.2 N ($\theta_0 = 0.30\pi$), respectively. The peak forces increased by 57.2%, 36.4%, and 16.4%, respectively, compared to the desired force value. Despite these variations, the recovery times were relatively consistent, at 1.280 s, 1.287 s, and 1.357 s, respectively. Compared with the most suitable mechanism configuration ($\theta_0 = 0.30\pi$) for the reference output force of 50 N (making it located in the low stiffness area), the peak force of the high stiffness configuration ($\theta_0 = 0.26\pi$) after a collision is 35.1% greater than that of the low stiffness configuration. The force recovery time of the low stiffness configuration increases by only 6.0%. This indicates that the softening stiffness profile maintains low stiffness behavior within the target force range, ensuring that there will be no significant fluctuations in the interaction force during unexpected collisions or shocks in human–robot interaction. Simultaneously, the low stiffness characteristic does not compromise the force control robustness of the SNEMA.

6. Application of the SNEMA in Centaur robot

The specific proposed SNEMA prototype is deployed in the Centaur robot to preliminarily demonstrate the practical application. The SNEMA is employed to connect the Centaur torso and the human, with the robotic torso serving as the input of the mechanism and the output of the mechanism being connected to the backpack worn by the human, as shown in Fig. 14(a). A preliminary experiment was conducted to demonstrate the advantages of the SNEMA in human–robot interaction control. The participant was asked to stand still while the Centaur robot was tested under SNEMA and rigid connection. Under the SNEMA condition, the mechanism's configuration was set to $\theta_0 = 0.30\pi$, and the desired interaction forces were 52 N and 30 N. In the case of rigid connection, the Centaur was commanded to walk in place, for an expected interaction force of 0 N in ideal situation.

The actual interaction force F during the experiment are illustrated in Fig. 14(b). It can be seen that force fluctuations are most drastic under the rigid connection, with a RMS deviation of 10.1401 N. This indicates that under high impedance conditions, the dynamic walking impact significantly affects the interaction force, making it challenging to stabilize. After employing SNEMA, the fluctuation in the interaction force between the Centaur and the human is significantly reduced, illustrating the effectiveness of SNEMA in compliant human–robot interaction. The force RMS errors for 52 N and 30 N are 2.5140 N and 4.4446 N, respectively. The accuracy improvement is attributed to softening stiffness characteristics, which increase force resolution at low stiffness range as the output force increases, thereby enhancing the force control accuracy. The results are consistent with the bench test, further validating the advantages of the proposed SNEMA for human–robot interaction force control.

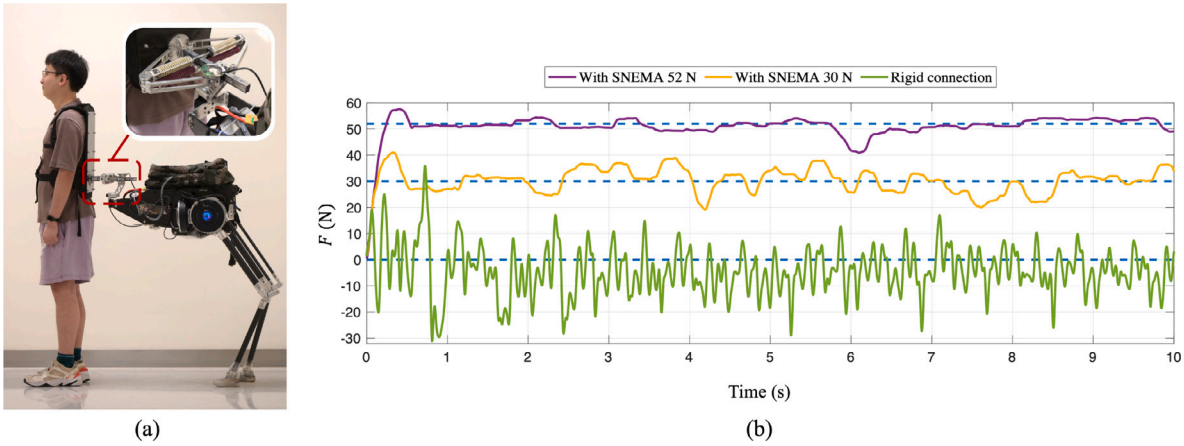

Fig. 14. Application of the SNEMA. (a) The human-Centaur system with SNEMA. (b) Experimental results of human-Centaur system interaction force control.

7. Discussion and conclusions

This work presents the stiffness modeling, physical implementation, and control strategy of a softening nonlinear-stiffness elastic mechanism with adjustability for human–robot interaction force control. A novel diamond-shaped mechanism equipped with an antagonistic-spring regulation mechanism is proposed to generate adjustable softening nonlinear force stiffness. This softening stiffness profile is strategically designed to balance the output force range and the force control accuracy in a compact structure. The utilization of two antagonistic compression springs realizes the continuous and convenient adjustment of the initial mechanism angle θ_0 of the SNEMA, thus achieving the adjustable stiffness profile to expand the output force range and achieve specialization of different tasks. Setting the output force to a suitable low stiffness area enhances force control precision and ensures the safety of human–robot interaction, diminishing the stringent demands on position control accuracy. The unique characteristics of the SNEMA are particularly beneficial for collaborative robots that interact with humans as an independent agent, such as the Centaur robot [14] and some other legged robots [8,10].

The softening nonlinear-stiffness profile is the main feature of the proposed SNEMA. The softening stiffness profile can improve the accuracy of the output force control of the elastic mechanism within a specific high output force range. Softening stiffness behavior means that the equivalent stiffness of the mechanism decreases with increasing output, displaying high stiffness at low output and low stiffness at high output. For static reference forces, such as step response, a higher force resolution can maintain a relatively high force control accuracy even when the position control accuracy is relatively lower. This characteristic is evident in the step force control experiment, as shown in Fig. 11(d)–(e). Across various mechanism configurations, the force control error diminishes as stiffness decreases. The reduction of force control RMS errors in the low stiffness area of the three different mechanism configurations are 66.2%, 29.0%, and 67.0%, respectively. This nonlinear-stiffness characteristic can improve the force resolution within the target output force range and achieve higher force control accuracy even with less precise position control. For non-constant tracking force trajectories, such as sinusoidal force, the relationship between stiffness reduction and accuracy improvement is not strictly monotonic, requiring a certain system bandwidth to ensure adequate tracking performance. This conclusion is confirmed by the sinusoidal tracking results, showing a U-shaped trend for force tracking accuracy with stiffness reduction. For the same reference sinusoidal force trajectory, the relatively low stiffness configuration reduces the error by 28.9% compared to the high stiffness configuration and 12.7% compared to the zero stiffness configuration. The low stiffness strikes a balance between force tracking performance and force resolution, resulting in better force control performance. The experimental results preliminarily confirm that the sinusoidal tracking accuracy in the low stiffness area (25%–50% K_m) is optimal.

The mechanical attribute of low stiffness plays a pivotal role in maintaining the safety of human–robot interaction, which is also one of the advantages of using softening stiffness characteristics in human augmentation robots. For the rigid human–robot interaction, in situations where the human experiences an emergency event, such as an abrupt stop or collision, the interaction force between the human and the robot may undergo a huge increase. This elevated force, originating from the inherent high impedance of rigid structures, poses potential risks to both the human body and the robot. As shown in Fig. 13(d), experimental results demonstrate that the proposed SNEMA exhibits low impedance characteristics in the event of a collision at the output end, with the output force experiencing only a 16.4% increase. In contrast, under high stiffness conditions, the force increases by 57.2%. Notably, the force recovery time after a collision shows no significant difference between low stiffness and high stiffness, with both returning to the desired force within 0.4 s after the collision.

Compared to the constant stiffness mechanism, softening stiffness profile also conserves the stroke of the elastic mechanism, which is a critical factor for robots with compact structure requirements. The proposed softening structure demonstrates high stiffness at low output, necessitating only a minimal compression stroke to attain the desired output force. According to the stiffness modeling of the SNEMA, as shown in Fig. 5(a), the nonlinear-stiffness profile can save up to 55% of the mechanism's stroke compared to

directly using a low stiffness linear spring to generate the same output force. This feature facilitates the designers in maintaining a more compact overall structure of the robot, which is particularly advantageous for integration within the Centaur robot.

While the proposed SNEMA exhibits promising potential for human–robot interaction force control, there are still several ideas for future exploration. In this study, the PD control parameters are constant to compare force control performance under different stiffness conditions. However, in practical scenarios, it might be beneficial to select the specific PD parameters for varying mechanism configurations and stiffness conditions. Future research will focus on developing an adaptive force controller that incorporates human motion feedforward terms, aiming to significantly improve both the force control performance and the assistance effectiveness on practical application platforms.

CRediT authorship contribution statement

Zhixin Tu: Writing – review & editing, Writing – original draft, Validation, Methodology, Investigation, Formal analysis, Conceptualization. **Haifeng Liu:** Validation, Methodology, Conceptualization. **Yihao Jiang:** Validation, Methodology, Investigation. **Tao Ye:** Validation, Methodology. **Yuepeng Qian:** Writing – review & editing, Investigation, Conceptualization. **Yuquan Leng:** Supervision, Conceptualization. **Jian S. Dai:** Writing – review & editing, Supervision. **Chenglong Fu:** Writing – review & editing, Supervision, Funding acquisition.

Declaration of competing interest

The authors declare that they have no known competing financial interests or personal relationships that could have appeared to influence the work reported in this paper.

Data availability

Data will be made available on request.

Acknowledgments

This work was supported in part by the Stable Support Plan Program of Shenzhen Natural Science Fund under Grant 20200925174640002 and the Science, Technology, and Innovation Commission of Shenzhen Municipality under Grant KCXFZ20230731093401004 and Grant ZDSYS20200811143601004.

References

[1] Wujing Cao, Chunjie Chen, Hongyue Hu, Kai Fang, Xinyu Wu, Effect of hip assistance modes on metabolic cost of walking with a soft exoskeleton, IEEE Trans. Autom. Sci. Eng. 18 (2) (2020) 426–436.
[2] Yixin Shao, Wuxiang Zhang, Yujie Su, Xilun Ding, Design and optimisation of load-adaptive actuator with variable stiffness for compact ankle exoskeleton, Mech. Mach. Theory 161 (2021) 104323.
[3] Tomislav Bacek, Marta Moltedo, Carlos Rodriguez-Guerrero, Joost Geeroms, Bram Vanderborght, Dirk Lefeber, Design and evaluation of a torque-controllable knee joint actuator with adjustable series compliance and parallel elasticity, Mech. Mach. Theory 130 (2018) 71–85.
[4] Yuepeng Qian, Shuaishuai Han, Yining Wang, Haoyong Yu, Chenglong Fu, Toward improving actuation transparency and safety of a hip exoskeleton with a novel nonlinear series elastic actuator, IEEE/ASME Trans. Mechatronics 28 (1) (2022) 417–428.
[5] Inseung Kang, Hsiang Hsu, Aaron Young, The effect of hip assistance levels on human energetic cost using robotic hip exoskeletons, IEEE Robot. Autom. Lett. 4 (2) (2019) 430–437.
[6] Tun Wang, Yen-Hua Lin, Emmanouil Spyrakos-Papastavridis, Sheng Quan Xie, Jian S Dai, Stiffness evaluation of a novel ankle rehabilitation exoskeleton with a type-variable constraint, Mech. Mach. Theory 179 (2023) 105071.
[7] Jody Alessandro Saglia, Nikolaos G Tsagarakis, Jian S Dai, Darwin G Caldwell, Control strategies for ankle rehabilitation using a high performance ankle exerciser, in: 2010 IEEE International Conference on Robotics and Automation, IEEE, 2010, pp. 2221–2227.
[8] Federico Parietti, Harry Asada, Supernumerary robotic limbs for human body support, IEEE Trans. Robot. 32 (2) (2016) 301–311.
[9] Zhixin Tu, Yijun Fang, Yuquan Leng, Chenglong Fu, Task-based human-robot collaboration control of supernumerary robotic limbs for overhead tasks, IEEE Robot. Autom. Lett. 8 (8) (2023) 4505–4512.
[10] Ming Hao, Jiwen Zhang, Ken Chen, Harry Asada, Chenglong Fu, Supernumerary robotic limbs to assist human walking with load carriage, J. Mech. Robot. 12 (6) (2020) 061014.
[11] Prokopios Antonellis, Arash Mohammadzadeh Gonabadi, Sara A Myers, Iraklis I Pipinos, Philippe Malcolm, Metabolically efficient walking assistance using optimized timed forces at the waist, Sci. Robot. 7 (64) (2022) eabh1925.
[12] Arash Mohammadzadeh Gonabadi, Prokopios Antonellis, Philippe Malcolm, A system for simple robotic walking assistance with linear impulses at the center of mass, IEEE Trans. Neural Syst. Rehabil. Eng. 28 (6) (2020) 1353–1362.
[13] Ping Yang, Haoyun Yan, Bowen Yang, Jianquan Li, Kailin Li, Yuquan Leng, Chenglong Fu, A centaur system for assisting human walking with load carriage, in: 2022 IEEE/RSJ International Conference on Intelligent Robots and Systems, IROS, IEEE, 2022, pp. 5242–5248.
[14] Haoyun Yan, Jianquan Li, Haifeng Liu, Zhixin Tu, Ping Yang, Muye Pang, Yuquan Leng, Chenglong Fu, Locomotion control on human-centaur system with spherical joint interaction, IEEE Robot. Autom. Lett. 9 (5) (2024) 4838–4845.
[15] Neville Hogan, Impedance control: An approach to manipulation, in: 1984 American Control Conference, IEEE, 1984, pp. 304–313.
[16] David J Braun, Vincent Chalvet, Tze-Hao Chong, Salil S Apte, Neville Hogan, Variable stiffness spring actuators for low-energy-cost human augmentation, IEEE Trans. Robot. 35 (6) (2019) 1435–1449.
[17] Haoyong Yu, Sunan Huang, Gong Chen, Yongping Pan, Zhao Guo, Human–robot interaction control of rehabilitation robots with series elastic actuators, IEEE Trans. Robot. 31 (5) (2015) 1089–1100.

[18] Emmanouil Spyrakos-Papastavridis, Jian S. Dai, A variable impedance scheme based on power-shaping signals and partial knowledge of link-side dynamics for flexible-joint robot interaction and tracking control, IEEE/ASME Trans. Mechatronics (2023).
[19] Gill A. Pratt, Matthew M. Williamson, Series elastic actuators, in: Proceedings 1995 IEEE/RSJ International Conference on Intelligent Robots and Systems. Human Robot Interaction and Cooperative Robots, Vol. 1, IEEE, 1995, pp. 399–406.
[20] Haoyong Yu, Sunan Huang, Gong Chen, Nitish Thakor, Control design of a novel compliant actuator for rehabilitation robots, Mechatronics 23 (8) (2013) 1072–1083.
[21] Haoran Zhong, Xinyu Li, Liang Gao, Congbo Li, Toward safe human–robot interaction: A fast-response admittance control method for series elastic actuator, IEEE Trans. Autom. Sci. Eng. 19 (2) (2021) 919–932.
[22] Tom Verstraten, Philipp Beckerle, Raphaël Furnémont, Glenn Mathijssen, Bram Vanderborght, Dirk Lefeber, Series and parallel elastic actuation: Impact of natural dynamics on power and energy consumption, Mech. Mach. Theory 102 (2016) 232–246.
[23] Gabriel Aguirre-Ollinger, Haoyong Yu, Lower-limb exoskeleton with variable-structure series elastic actuators: Phase-synchronized force control for gait asymmetry correction, IEEE Trans. Robot. 37 (3) (2021) 763–779.
[24] Zhibin Song, Shaobin Lan, Jian S. Dai, A new mechanical design method of compliant actuators with non-linear stiffness with predefined deflection-torque profiles, Mech. Mach. Theory 133 (2019) 164–178.
[25] Xiuqi Hu, Zhibin Song, Tianyu Ma, Novel design method for nonlinear stiffness actuator with user-defined deflection-torque profiles, Mech. Mach. Theory 146 (2020) 103712.
[26] Sebastian Wolf, Giorgio Grioli, Oliver Eiberger, Werner Friedl, Markus Grebenstein, Hannes Höppner, Etienne Burdet, Darwin G Caldwell, Raffaella Carloni, Manuel G Catalano, et al., Variable stiffness actuators: Review on design and components, IEEE/ASME Trans. Mechatronics 21 (5) (2015) 2418–2430.
[27] Yapeng Xu, Kai Guo, Jie Sun, Jianfeng Li, Design, modeling and control of a reconfigurable variable stiffness actuator, Mech. Syst. Signal Process. 160 (2021) 107883.
[28] Xiantao Sun, Xiaoyu Xiong, Wenjie Chen, Weihai Chen, Guilin Yang, Design and control of a novel variable stiffness actuator based on antagonistic variable radius principle, ISA Trans. (2024).
[29] Amir Jafari, Nikos G. Tsagarakis, Darwin G. Caldwell, A novel intrinsically energy efficient actuator with adjustable stiffness (AwAS), IEEE/ASME Trans. Mechatronics 18 (1) (2011) 355–365.
[30] Jiantao Sun, Zhao Guo, Yubing Zhang, Xiaohui Xiao, Jianrong Tan, A novel design of serial variable stiffness actuator based on an archimedean spiral relocation mechanism, IEEE/ASME Trans. Mechatronics 23 (5) (2018) 2121–2131.
[31] Yixin Shao, Di Shi, Yanggang Feng, Wuxiang Zhang, Xilun Ding, Design and control of a compact variable stiffness actuator based on a cam-circular beam mechanism, IEEE/ASME Trans. Mechatronics (2024).
[32] Yuepeng Qian, Shuaishuai Han, Gabriel Aguirre-Ollinger, Chenglong Fu, Haoyong Yu, Design, modeling, and control of a reconfigurable rotary series elastic actuator with nonlinear stiffness for assistive robots, Mechatronics 86 (2022) 102872.
[33] Zhongyi Li, Shaoping Bai, A novel revolute joint of variable stiffness with reconfigurability, Mech. Mach. Theory 133 (2019) 720–736.
[34] F Aimedee, Grigore Gogu, Jian S Dai, C Bouzgarrou, N Bouton, Systematization of morphing in reconfigurable mechanisms, Mech. Mach. Theory 96 (2016) 215–224.
[35] Pengjie Xiang, Liang Yan, Yiming Guo, Xinghua He, Chris Gerada, I-Ming Chen, A concentrated-flux-type pm machine with irregular magnets and iron poles, IEEE/ASME Trans. Mechatronics 29 (1) (2024) 691–702.
[36] Shuuji Kajita, Bernard Espiau, Legged robot, in: Springer Handbook of Robotics, Springer Berlin/Heidelberg, Germany, 2008, pp. 361–389.
[37] Jung-Jun Park, Yong-Ju Lee, Jae-Bok Song, Hong-Seok Kim, Safe joint mechanism based on nonlinear stiffness for safe human-robot collision, in: 2008 IEEE International Conference on Robotics and Automation, IEEE, 2008, pp. 2177–2182.
[38] John G.P. Barnes, An algorithm for solving non-linear equations based on the secant method, Comput. J. 8 (1) (1965) 66–72.
[39] DA Neumann, ER Kelly, CL Kiefer, K Martens, CM Grosz, Kinesiology of the Musculoskeletal System: Foundation for Rehabilitation, 3rd ed., Vol. 350, Mosby Elsevier, St. Louis, MO, 2017, p. 368.